Measuring Turbulent Kinetic Energy Dissipation at a Wavy Sea Surface

PETER SUTHERLAND* AND W. KENDALL MELVILLE

Scripps Institution of Oceanography, La Jolla, California

(Manuscript received 15 December 2014, in final form 23 April 2015)

ABSTRACT

Wave breaking is thought to be the dominant mechanism for energy loss by the surface wave field. Breaking results in energetic and highly turbulent velocity fields, concentrated within approximately one wave height of the surface. To make meaningful estimates of wave energy dissipation in the upper ocean, it is then necessary to make accurate measurements of turbulent kinetic energy (TKE) dissipation very near the surface. However, the surface wave field makes measurements of turbulence at the air–sea interface challenging since the energy spectrum contains energy from both waves and turbulence over the same range of wavenumbers and frequencies. Furthermore, wave orbital velocities can advect the turbulent wake of instrumentation into the sampling volume of the instrument. In this work a new technique for measuring TKE dissipation at the sea surface that overcomes these difficulties is presented. Using a stereo pair of longwave infrared cameras, it is possible to reconstruct the surface displacement and velocity fields. The vorticity of that velocity field can then be considered to be representative of the rotational turbulence and not the irrotational wave orbital velocities. The turbulent kinetic energy dissipation rate can then be calculated by comparing the vorticity spectrum to a universal spectrum. Average surface TKE dissipation calculated in this manner was found to be consistent with near-surface values from the literature, and time-dependent dissipation was found to depend on breaking.

1. Introduction

Wind flowing over the open ocean creates surface waves. Fluxes of energy, momentum, and mass between the atmosphere and ocean are all modulated by the waves, and in particular by wave breaking (Melville 1996). Some of the energy and momentum input by the wind propagates away from the input region through swell, but the majority is transferred to the water column locally, resulting in a turbulent near-surface marine boundary layer. This work is a description of a new technique for the measurement of turbulent kinetic energy (TKE) at the sea surface in the presence of surface waves.

There is considerable evidence in the literature for increased TKE dissipation near the sea surface over that predicted by the "law of the wall" (Kitaigorodskii et al. 1983; Gargett 1989; Agrawal et al. 1992; Anis and Moum 1992; Osborn et al. 1992; Melville 1994; Terray et al. 1996; Drennan et al. 1996; Gemmrich 2010). However, traditional measurements of dissipation, and turbulence in general, very near the surface of the ocean are notoriously difficult, and thus the structure of the turbulence very near the surface remains an outstanding question.

The greatest source of difficulty in measuring turbulence near the sea surface is the surface wave field. The new technique presented in this work addresses the two principal measurement challenges presented by surface waves: 1) Waves represent an unsteady velocity field at the same scales as the turbulence, meaning that wave motions are difficult to separate from turbulence. 2) Wave orbital motions can advect the wake of an instrument through the instrument's sampling volume, making it difficult to separate the turbulent wake from the background ocean turbulence being measured.

The separation of waves and turbulence is a problem that permeates many areas of geophysical fluid dynamics, especially field measurements in physical oceanography and meteorology (e.g., Kitaigorodskii et al. 1983; Soloviev et al. 1988; Trowbridge 1998). Many methods depend on spectral separation of waves and turbulence (e.g., Stewart and Grant 1962; Lumley and Terray 1983), but frequently, particularly at the sea surface, the scales of turbulence and

* Current affiliation: Laboratoire d'Océanographie et du Climat, Université Pierre et Marie Curie, Paris, France.

Corresponding author address: Peter Sutherland, Laboratoire d'Océanographie et du Climat, Université Pierre et Marie Curie, 4 Place Jussieu, 75005 Paris, France.
E-mail: peter.sutherland@locean-ipsl.upmc.fr

DOI: 10.1175/JTECH-D-14-00227.1

wave motions in space and time overlap to such a degree that this is not useful. At the sea surface, it is tempting to assume all velocities that are coherent with fluctuations of the surface displacement are wave motion and that the remainder is turbulence. However, this eliminates the possibility of measuring wave-modulated turbulence.

Another important consideration whenever any instrument that samples turbulence is deployed in a wavy environment is the great difficulty in ensuring that the instrument is not sampling its own wake (Gerbi et al. 2009). The wave field in the open sea often has a broad directional distribution, making it difficult to ensure that the sampling volume is not sometimes ''downstream'' of the instrument itself. This interference can occur multiple times modulo a close approximation to the wave period, depending on the relative strength of the current and the Stokes drift, versus the wave orbital velocity. Previous authors have typically avoided this difficulty by carefully selecting data at times when the mean velocity is sufficiently larger than the wave-orbital velocities (Gerbi et al. 2009). Unfortunately, this criterion is seldom met very near the sea surface.

Recent advances in infrared (IR) imaging and image analysis have provided a new way to measure the velocity of the fluid at the sea surface that entirely removes the danger of instrument wake contamination. Using IR video imagery of the sea surface, taken from above the water surface, various authors, (e.g., Garbe et al. 2003; Veron et al. 2008; Rocholz et al. 2011; Chickadel et al. 2011) have shown that by treating the surface temperature structure as a passive tracer, tracking thermal features between video frames can yield a surface velocity field. Work by Chickadel et al. (2011) showed that it is possible to use that velocity field to measure TKE dissipation at the surface. They took frequency (σ) spectra of those velocities, found a $\sigma^{-5/3}$ inertial subrange and, assuming Taylor's frozen turbulence hypothesis and a Kolmogorov inertial subrange (Tennekes and Lumley 1972), were able to calculate dissipation. However, their measurements were taken on a river during a period when, in their own words, surface waves (which can contaminate turbulence estimates) were negligible.

In this work, a new analysis technique, based on stereo thermal imaging pattern image velocimetry (PIV), was developed to allow measurement of TKE dissipation in the presence of surface waves. By taking the vorticity of the measured surface velocity field, it was possible to isolate the rotational component of the flow, taken to be representative of the turbulence, and to remove the effects of the irrotational wave field. Vorticity spectra were then used to calculate TKE dissipation at the sea surface over the same range of scales as the surface waves. Thus, we present a technique that removes the two principle difficulties of measuring TKE dissipation at the sea surface.

The paper has been organized as follows. Section 2 describes the measurements, including descriptions of the platform, field sites, instrumentation, and stereo IR PIV processing. Section 3 describes the calculation of surface vorticity. Section 4 describes the technique for calculating TKE dissipation. Section 5 is a discussion of the results, including a comparison of results with the literature, a note on the wave coherence of surface dissipation, and a description of alternate techniques for calculating dissipation. Conclusions are in section 6. Sutherland and Melville (2015) combine the surface dissipation measurements described in this work with subsurface measurements to calculate total near-surface TKE dissipation.

2. Measurements

The data described here were collected during three deployments of Research Platform (R/P) *Floating Instrument Platform* (*FLIP*) in the Pacific Ocean: one in 2009 and two in 2010. *FLIP* was chosen as a platform because of its stability (Smith and Rieder 1997) and small water plane, which minimize reflection and shadowing of the wave field. Further, *FLIP* also has a small superstructure for minimal airflow distortion and long booms to hold instruments well away from the flow-distorted regions (Mollo-Christensen 1968).

a. Field sites

Three experimental locations were chosen to provide a wide range of environmental conditions; the trade wind–dominated region south of Hawaii, the strong alongshore winds off Northern California, and the relatively mild conditions in the Southern California Bight.

The first experiment, the Office of Naval Research's (ONR) Radiance in a Dynamic Ocean (RaDyO) 2009, (Dickey et al. 2012), was a 12-day deployment that started 120 km south of the island of Hawaii with *FLIP* drifting west at approximately 35 cm s^{-1} for approximately 330 km in trade winds.

The ONR-sponsored High Resolution Air–Sea Interaction (HiRes) Departmental Research Initiative (DRI) consisted of two experiments: HiRes 2010 was a 14-day deployment with *FLIP* moored approximately 25 km off the coast of Northern California (38°20′N, 123°26′W) in strong northwesterly winds. SoCal 2010 took place over 2 days in the Southern California Bight in much milder conditions.

Between the three experiments, 70 records, each 20 min in duration, were analyzed with 10-m wind speeds U_{10} = 1.6–16 m s^{-1}, significant wave heights H_s = 0.7–4.7 m,

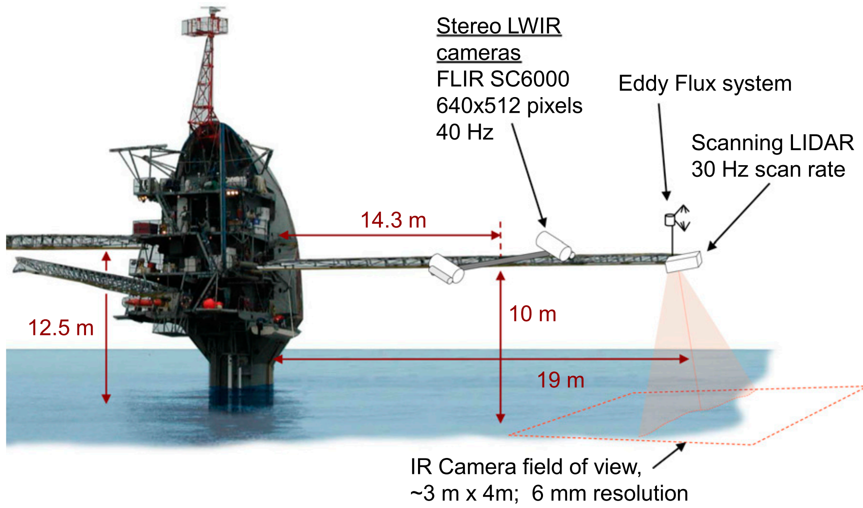

FIG. 1. Schematic of the instrument configuration on the starboard boom of R/P *FLIP* during the SoCal 2010 and HiRes 2010 experiments. The configuration during the RaDyO 2009 experiment was similar, but instruments were mounted on the opposite (port) boom.

and wave ages $c_m/u_* = 16$–150. Here, u_* is the atmospheric friction velocity and c_m is the spectral mean wave phase speed, related to the mean radian frequency σ_m using the linear deep-water dispersion relation $c_m = g/\sigma_m$, where g is gravitational acceleration. The omnidirectional frequency spectrum $S_{\eta\eta}(\sigma)$ was used to define

$$\sigma_m = \frac{\int_0^\infty \sigma S_{\eta\eta}(\sigma)\, d\sigma}{\int_0^\infty S_{\eta\eta}(\sigma)\, d\sigma}. \tag{1}$$

This integral measure of spectral wave speed was chosen due to the multimodal spectra present during the field experiments. Throughout these experiments, wind speed and wave age displayed a strong negative correlation, reducing the available parameter space significantly.

A more thorough description of the experimental conditions is given in Sutherland and Melville (2015).

b. Instrumentation

Each of the three experiments differed slightly in the instruments deployed and their configuration. Figure 1 shows a schematic of the instrument setup during the SoCal 2010 and HiRes 2010 experiments. The RaDyO 2009 instrument suite was similar, but it was installed on the port boom (instead of the starboard boom, as shown in the figure).

The primary instrumentation was a pair of FLIR SC6000 longwave infrared (8–9.2 μm) video cameras. The cameras were mounted 3 m apart on a horizontal spar near the end of one of *FLIP*'s booms. The cameras were angled slightly toward each other, so that they shared the same field of view on the sea surface, and angled 20° from vertical away from the hull of *FLIP* in order to reduce reflections from *FLIP*'s superstructure and booms. The collocated field of view at the surface was approximately 4 m $\times$ 3 m and the image size of 640 $\times$ 512 pixels resulted in a nominal resolution of approximately 6 mm (which changed depending on the instantaneous displacement of the surface relative to the boom). IR video was captured at 40 Hz (subsampled at 20 Hz) for the first 20 min of every hour.

In all three experiments, a Campbell Scientific eddy flux system (CSAT3 3D sonic anemometer) was mounted directly above the IR cameras' field of view. These data were processed to retrieve Reynolds stresses, wind speed, and wind direction, over 30-min averaging periods.

Subsurface turbulence was measured using an array of pulse-coherent acoustic Doppler devices. Those measurements are discussed in Sutherland and Melville (2015).

c. Stereo IR PIV analysis

Stereo imagery is a technique for three-dimensional (3D) scene reconstruction based on two-dimensional (2D) imagery. A detailed treatment of 3D computer vision is given by Ma et al. (2004). Stereo imagery uses image pairs taken by two cameras with a known relative position and orientation (separation and rotation). By matching features in both images, it is possible to triangulate their location in 3D. Tracking features in temporally consecutive images then allows the 3D velocity of the features to be calculated.

Over the duration of these experiments, the sea surface contained a wide variety of thermal structures.

Actively breaking waves, remnants of past breakers, and the surface signatures of turbulence all produce thermal patterns on millimeter to meter and larger length scales. When the temperature differences across these features were greater than the detectable minimum of the IR camera (>25 mK), they could be imaged and used for stereo PIV.

Stereo imaging of the sea surface is not new (see, e.g., Shemdin et al. 1988; Banner et al. 1989; Benetazzo 2006). The use of stereo IR imagery in the laboratory (Hilsenstein 2005) has shown it to be an effective way of eliminating the principal difficulties of using visible stereo on a water surface, namely, water penetration and specular reflection (Jähne et al. 1994). The experiments described here are, to the best of our knowledge, the first use of stereo infrared imagery to reconstruct the sea surface.

Stereo PIV has been used by other authors to study the velocity field at the surface. For example, Turney et al. (2009) used two video cameras to track particles in wave tank seeded with fluorescent microspheres. In contrast, the work presented here does not require seeding and is instead based on thermal structure PIV. Past uses of thermal structure PIV (e.g., Garbe et al. 2003; Veron et al. 2008; Rocholz et al. 2011; Chickadel et al. 2011) used a single IR camera and either assumed a flat sea surface to measure velocity or measured the projected horizontal component of velocity. To the best of our knowledge, thermal structure PIV has never been combined with stereo imaging to reconstruct the 3D velocity at the wavy sea surface.

The stereo PIV measurements resulted in an unevenly spaced grid with approximately 5-cm resolution over a patch of the sea surface covering approximately 2 m × 2 m. This field was sampled at 4 Hz. The sequence used for analysis of these data is given in the appendix.

3. Surface vorticity

Helmholtz's theorem states that any vector field, in this case the velocity $\mathbf{u}$, can be separated into irrotational $\mathbf{u}_I$ (curl free), and rotational $\mathbf{u}_R$ (divergence free), components:

$$\mathbf{u} = \underbrace{-\nabla\phi}_{\mathbf{u}_I} + \underbrace{\nabla\times\mathbf{A}}_{\mathbf{u}_R}, \qquad (2)$$

where ϕ is a scalar potential and $\mathbf{A}$ is a vector potential. The vorticity field,

$$\boldsymbol{\omega} = \nabla\times\mathbf{u}, \qquad (3)$$

then depends, by definition, on only the rotational velocity field.

Noting that surface waves are generally assumed to be irrotational to leading order and that turbulence is by definition rotational, the rotational component of velocity can be assumed to be representative of turbulence only, and not surface waves (Kitaigorodskii and Lumley 1983). Thus, it is possible to use statistics of the vorticity field to study turbulence in the flow.

a. Vorticity calculation

As outlined in section 2c, the end result of the stereo PIV processing is an irregularly spaced grid of points in 3D space, representing the sea surface position, with a three-component velocity vector assigned to each point, representing the surface velocity. The vorticity directed in the local surface-normal direction was calculated by measuring the circulation around each stereo velocity measurement point. Stokes's theorem says that for a closed loop, the vorticity flux through the loop is equal to the circulation around the perimeter of the loop. For a discrete set of N points, $\mathbf{p}_i$, on a closed loop, with associated velocities $\mathbf{u}_i$, the circulation can be approximated by

$$\Gamma = \sum_{i=1}^{N-1}\left(\frac{\mathbf{u}_i+\mathbf{u}_{i+1}}{2}\right)\cdot(\mathbf{p}_{i+1}-\mathbf{p}_i). \qquad (4)$$

Here, the closure of the material loop has been defined such that $\mathbf{p}_1 = \mathbf{p}_N$. A plane with normal vector $\hat{\mathbf{n}}$ is then fitted to those points. The surface area A contained by the projection of those points onto that plane, is used to calculate vorticity,

$$\boldsymbol{\omega}(\mathbf{p}) = \frac{\Gamma}{A}\hat{\mathbf{n}}. \qquad (5)$$

This vorticity calculation was performed for every point on each reconstructed velocity field and resulted in a vorticity resolution of approximately 15 cm (vorticity resolution is approximately one-third of the velocity resolution, 5 cm, which is set by the cross-correlation windows' size described in the appendix).

b. Surface vorticity associated with wave breaking

Breaking waves at the sea surface have been shown to create coherent vortices in laboratory experiments (Melville et al. 2002). Pizzo and Melville (2013) formalized a theoretical description of deep-water breaking waves as half vortex rings, the surface expression of which being a pair of counterrotating vortices at each end of the breaking front.

Figures 2a–c show examples of thermal imagery of breaking waves with the horizontal component of surface velocity overlaid. Figures 2d–f show the corresponding

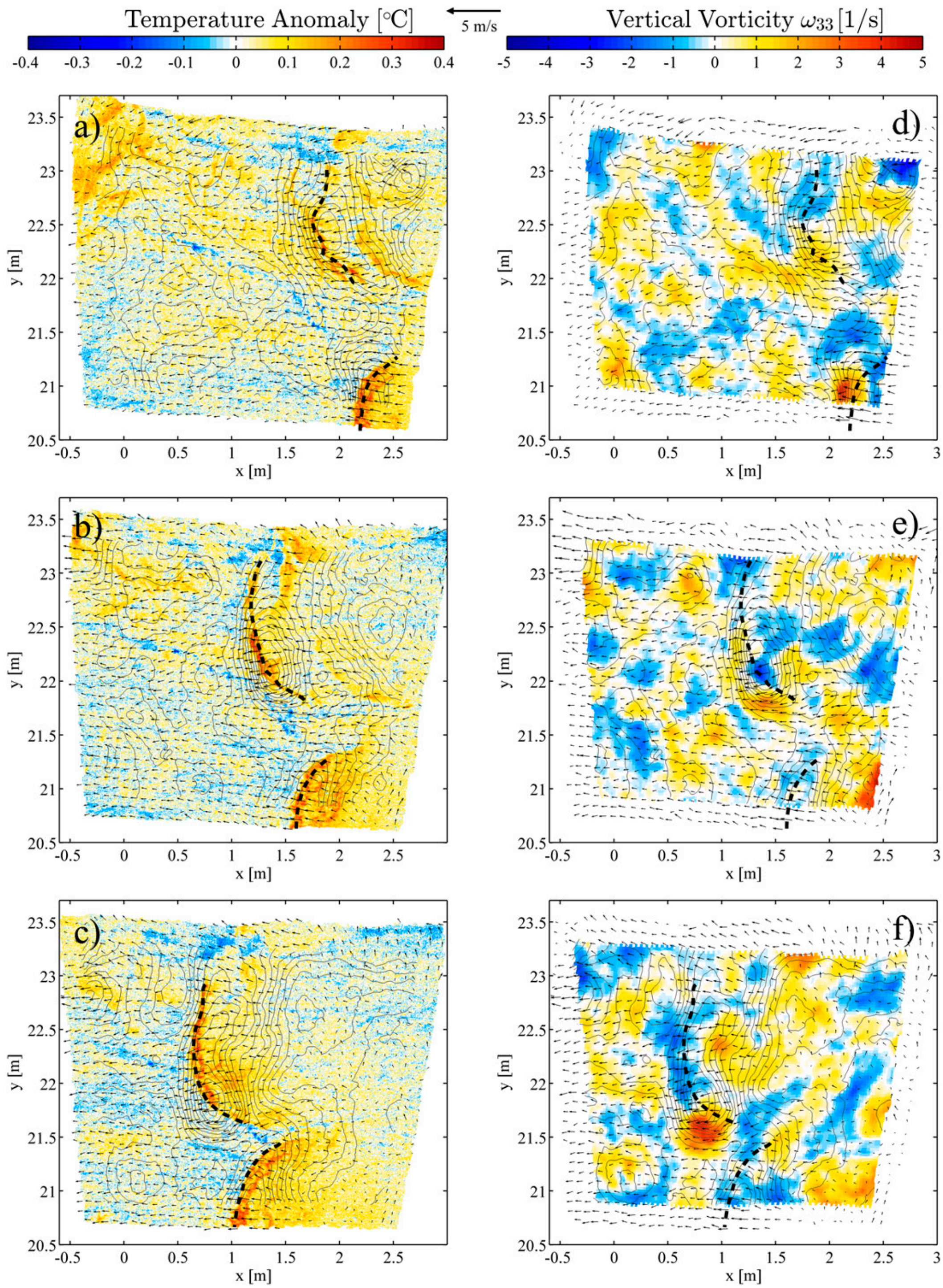

FIG. 2. Examples of propagating breaking waves in plan view: (a)–(c) temperature anomalies of the surface and (d)–(f) vertical vorticity at the surface. Panels (a) and (d) were taken at 1107:29.25 UTC 8 Sep 2009, during RaDyO 2009; (b) and (e) were taken 0.25 s later, at 1107:29.50 UTC; and (c) and (f) were taken 0.25 s after that, at 1107:29.75 UTC. The breaking fronts can be clearly seen in the temperature anomaly, propagating from left to right of the images, and are marked by the thick dashed black lines. In all panels, the surface velocity field is indicated by black arrows and gray contours. The black arrows are the scaled vector velocity (the small example arrow at the top of the figure indicates 5 m s^{-1}), and the gray contours are the speed, with each contour representing 0.1 m s^{-1}. The vorticity field and speed contours have been filtered with a 20-cm circular filter to highlight larger-scale features.

vertical vorticity fields, again with velocity overlaid. The expected vortex pairs can be seen attached to the upper of the two breakers in Fig. 2 (the breaker in the region $y = 21.5$–23 m), surrounding the peak in the breaking crest velocity. They appear as negative vertical vorticity on the right side of the breaker, when traveling in the direction of the breaker, and positive vorticity on the left. The lower breaker in Fig. 2 does not show a vortex pair as clearly because the lower half of that breaker is out of the image.

c. *Vorticity spectra*

Vorticity fields were regridded to a uniform grid (see the appendix, step 8), and directional wavenumber spectra of vorticity were then calculated. Figure 3 shows two examples of such spectra. Particularly notable is the "lobed" structure, orthogonal to the direction of wave propagation in Fig. 3a. This structure was found by Veron et al. (2009) to be consistent with the presence of wind rows, small features related to Langmuir circulations. Spectra indicating such streaks were not, however, universally found.

In this work, the departure from isotropy of each spectrum is defined by

$$\gamma_D = \frac{\phi_{\omega_3}(k_{\max}, \theta_{\max})}{\frac{1}{2\pi}\int_0^{2\pi} \phi_{\omega_3}(k_{\max}, \theta)\, d\theta} - 1, \qquad (6)$$

where $\phi_{\omega_3}(k, \theta)$ is the horizontal spectrum of vertical vorticity, written as a function of wavenumber k and azimuth angle θ. The wavenumber and azimuth of the spectral peak found in the 2D vorticity spectra are $k_{\max}$ and $\theta_{\max}$, respectively. In these experiments, γ_D was small, with an average value during RaDyO 2009 of $\gamma_D = 0.08$ and during SoCal 2010 of $\gamma_D = 0.23$.

Figure 4 gives an example of the difference between spectra of surface-normal vorticity and the vertical component of vorticity. The spectra for both types of vorticity exhibit the same slightly lobed structure, with the vorticity variance approximately 2.3% lower for the vertical vorticity than the surface-normal vorticity. The effects of these differences on the calculation of TKE dissipation discussed in section 4 were not found to be significant.

4. Surface TKE dissipation

The major motivation for this work has been to measure TKE dissipation rate at the sea surface. TKE dissipation is defined as $\varepsilon \equiv 2\nu\langle s_{ij}s_{ij}\rangle$, where $s_{ij} \equiv 1/2(\partial u_i/\partial x_j + \partial u_j/\partial x_i)$ is the rate of strain tensor

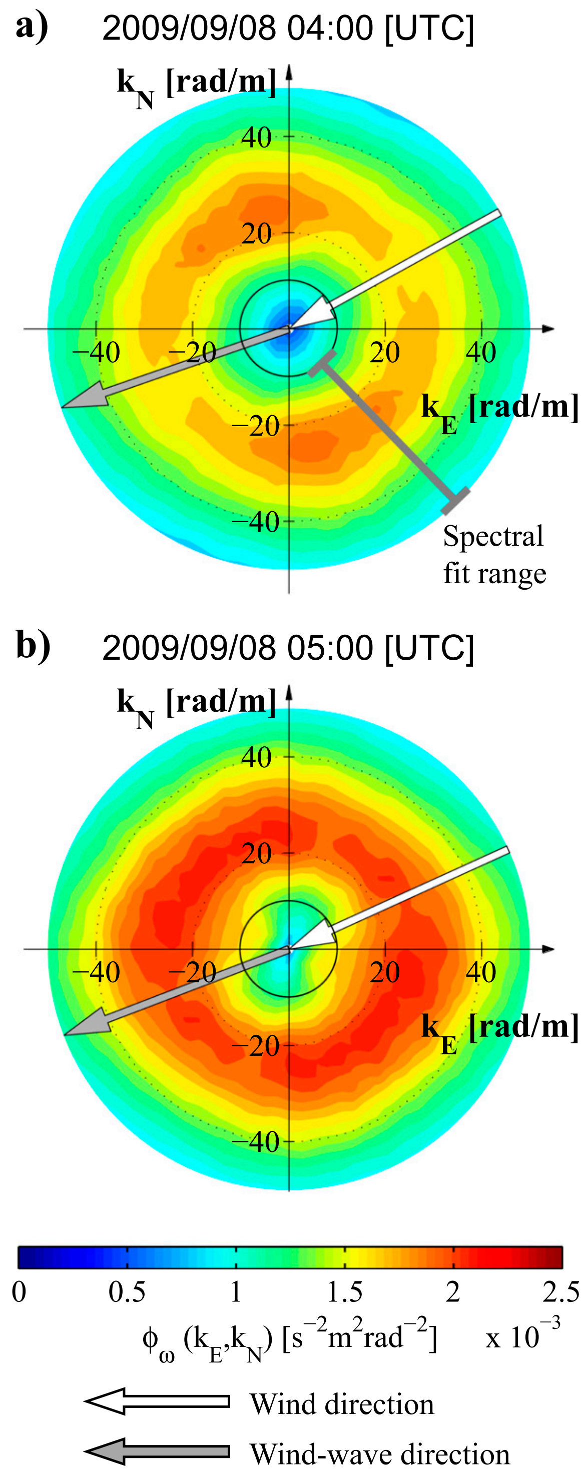

FIG. 3. The 20-min average directional wavenumber spectra of vertical vorticity $\phi_{\omega_3}(k_E, k_N)$ taken during RaDyO 2009, and separated by 1 h: (a) taken starting 0400 UTC 8 Sep 2009 and (b) taken starting 0500 UTC 8 Sep 2009. White arrows show the mean wind direction, gray arrows show the direction of the wind-wave spectral peak, and solid black circles show $k = 10$ rad m^{-1}. The gray bar in (a) indicates the range of wavenumbers used for the spectral fitting in the calculation of surface TKE dissipation, as described in section 4 (the wavenumber range is also shown in Fig. 7).

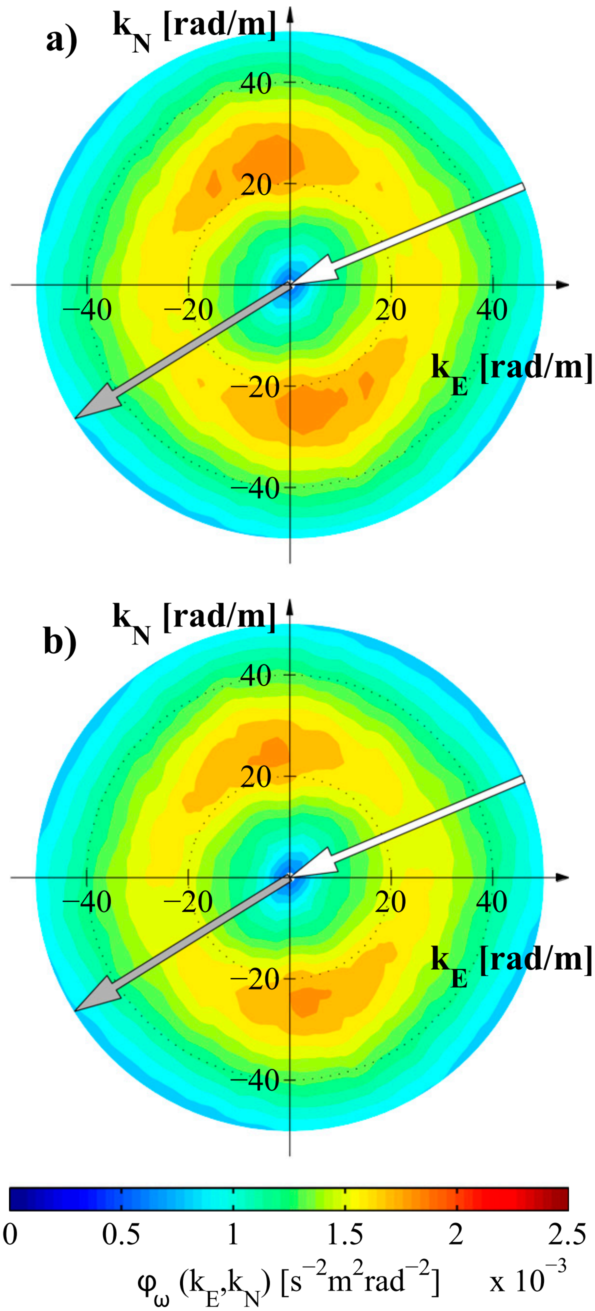

FIG. 4. Comparison of surface-normal and vertical vorticity. Spectra are both for the same 20-min averaging period, and are of (a) surface-normal vorticity and (b) vertical component of surface-normal vorticity. Sampling period started at 0300 UTC 8 Sep 2009 during RaDyO 2009.

and ν is the kinematic viscosity. At high Reynolds numbers, this can be approximated as $\varepsilon \cong \nu\langle\omega_i\omega_i\rangle$ (Tennekes and Lumley 1972). This provides a means of accessing dissipation directly from the vorticity or velocity fields, but it requires the resolution of the Kolmogorov microscale, which is smaller than the PIV resolution available in these field measurements.

In this work, a technique has been developed for measuring surface dissipation based on the vorticity spectrum at scales larger than the Kolmogorov microscale. The data processing scheme is discussed in detail below, but in summary it consists of calculating the vorticity spectrum of the data, calculating a theoretical vorticity spectrum based on dissipation ε and subject to gridding effects, and then varying ε to minimize the difference between the theoretical spectrum and the measured spectrum.

In a process somewhat analogous to the $k^{-5/3}$ inertial subrange slope-fitting technique commonly used to measure TKE dissipation in turbulent flows (Tennekes and Lumley 1972), it is possible to use the universal form of the vorticity spectrum to estimate dissipation. Assuming homogeneous isotropic turbulence, and following Antonia et al. (1988), the two-dimensional wavenumber spectrum of vorticity can be written as

$$\phi_{\omega_3}(k_1,k_2) = \int_{-\infty}^{\infty} \frac{E(k)}{4\pi}\left(1-\frac{k_3^2}{k^2}\right) dk_3, \tag{7}$$

where $E(k)$ is the energy spectrum function; k_1, k_2, and k_3 are the three orthogonal components of the wavenumber $\mathbf{k}$; and $k = |\mathbf{k}|$. The spectrum is then of ω_3, the component of the vorticity vector in the direction of k_3. Equation (7) can then be integrated to give the one-dimensional spectrum of vorticity,

$$\phi_{\omega_3}(k_1) = \int\int_{-\infty}^{\infty} \frac{E(k)}{4\pi}\left(1-\frac{k_3^2}{k^2}\right) dk_2\, dk_3. \tag{8}$$

For this work, k_1 and k_2 are in orthogonal horizontal directions, and k_3 points vertically upward, meaning that Eqs. (7) and (8) give horizontal spectra of vertical vorticity.

A classical form for the energy spectrum function is given in Pope (2000, 232–233),

$$E(k) = C\varepsilon^{2/3}k^{-5/3}f_\eta(k\eta), \tag{9}$$

where the rolloff at the Kolmogorov scale follows the form

$$f_\eta(k\eta) = \exp(-\beta\{[(k\eta)^4 + c_\eta^4]^{1/4} - c_\eta\}). \tag{10}$$

In this work, it was assumed that the outer scale of turbulence was much larger than the camera field of view. The Kolmogorov scale is defined as $\eta \equiv (\nu^3/\varepsilon)^{1/4}$;

the value for the constant $\beta = 5.2$ is taken from the literature, for example, Saddoughi and Veeravalli (1994); and the constant $c_\eta \approx 0.4$ is determined by requiring $\varepsilon = \int_0^\infty 2\nu k^2 E(k)\,dk$ (again, see Pope 2000, 232–233).

Numerical solutions for the form of vertical vorticity spectra given in Eq. (8), using the energy spectrum from Eq. (9), are plotted in Fig. 5 for dissipation levels varying over five orders of magnitude.

The effects of gridding the data have been simulated by replacing the raw measured 3D velocity field with a synthetic one consisting of random white noise; this synthetic velocity field was then regridded and used to calculate vorticity following the same technique as for the actual measured velocity field. The 2D spectrum of this regridded random white vorticity field $S_{\mathrm{WHT}}(k_1, k_2)$ was then scaled so that it reached a maximum value of unity, and was taken to represent the spectral rolloff due to regridding,

$$S_{\mathrm{roll}}(k_1, k_2) = \frac{S_{\mathrm{WHT}}(k_1, k_2)}{\max[S_{\mathrm{WHT}}(k_1, k_2)]}. \tag{11}$$

In the work presented here, $S_{\mathrm{roll}}(k_1, k_2)$ is nearly isotropic (see Fig. 6b) due to the relatively uniform sampling of vorticity. However, it is important to note that isotropy of $S_{\mathrm{roll}}(k_1, k_2)$ is not a feature of all sampling schemes.

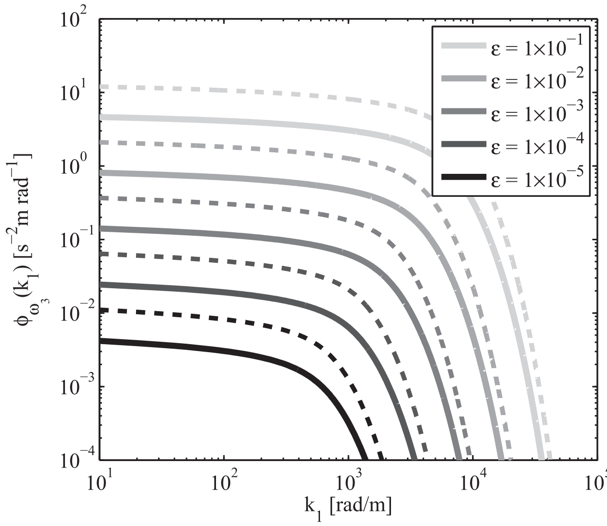

FIG. 5. Numerical solutions of theoretical k_1 vorticity spectra for 3D (solid line) and 2D (dashed line) isotropic turbulence, corresponding to Eqs. (8) and (14), respectively. Energy spectra used are of the form given in Eq. (9). The gray scale indicates dissipation (m^2 s^{-3}). For any fixed wavenumber k_1 over the range $1 \le k_1 \le 400$, the spectral level at that wavenumber $\phi_{\omega_3}(k_1)$ varies with dissipation as approximately $\phi_{\omega_3}(k_1) \sim \varepsilon^{0.8}$.

Multiplying the theoretical spectrum $\phi_{\omega_3}(k_1, k_2)$ from Eq. (7), subject to Eq. (9), by the scaled 2D spectrum of white noise $S_{\mathrm{roll}}(k_1, k_2)$ gave the final modeled vorticity spectrum for any prescribed dissipation value,

$$S_{\mathrm{MOD}}(\varepsilon; k_1, k_2) = S_{\mathrm{roll}}(k_1, k_2)\int_{-\infty}^{\infty} \frac{C\varepsilon^{2/3}k^{-5/3}f_\eta(k\eta)}{4\pi}\left(1 - \frac{k_3^2}{k^2}\right)dk_3. \tag{12}$$

Dissipation was then varied to minimize the difference (via a least squares cost function) between $S_{\mathrm{MOD}}(\varepsilon; k_1, k_2)$ and the measured spectrum. A schematic of this processing sequence is given in Fig. 6. Examples of one-dimensional measured vorticity spectra are shown as black dashed lines in Fig. 7. The corresponding 1D fit spectra,

$$S_{\mathrm{MOD}}(\varepsilon; k_1) = \int_{-\infty}^{\infty} S_{\mathrm{MOD}}(\varepsilon; k_1, k_2)\,dk_2, \tag{13}$$

are shown as the solid gray curves and the wavenumber range of that fitting, $10 < k < 50$ rad m^{-1}, is highlighted in light gray. The fitting range corresponds to the whole range of wavenumbers plotted in Fig. 3, with the exception of the regions enclosed by the solid black circles ($k < 10$ rad m^{-1}). This spectral range was chosen to capture the peaks of the vorticity spectra without extending to scales larger than were reliably captured in the regridded vorticity data or extending to scales smaller than the velocity resolution. Measured dissipation levels were found to be relatively insensitive to the spectral fit range due to the very strong dependence of dissipation on spectral level (see Fig. 5).

Sources of error

It is important to note that this calculation is based on the assumption of 3D homogeneous isotropic turbulence. This argument would be completely valid if the velocity field used were from a 2D slice through the center of such turbulence, but it is somewhat questionable when the surface velocity field is used. Potential effects of the free surface on the underlying 3D turbulence must be considered. Numerical work has shown a suppression of vertical turbulent velocity variance near a free surface (e.g., Shen and Yue 2001). A similar behavior has been observed in highly stratified atmospheric flows (Lindborg 2007). The limiting case of

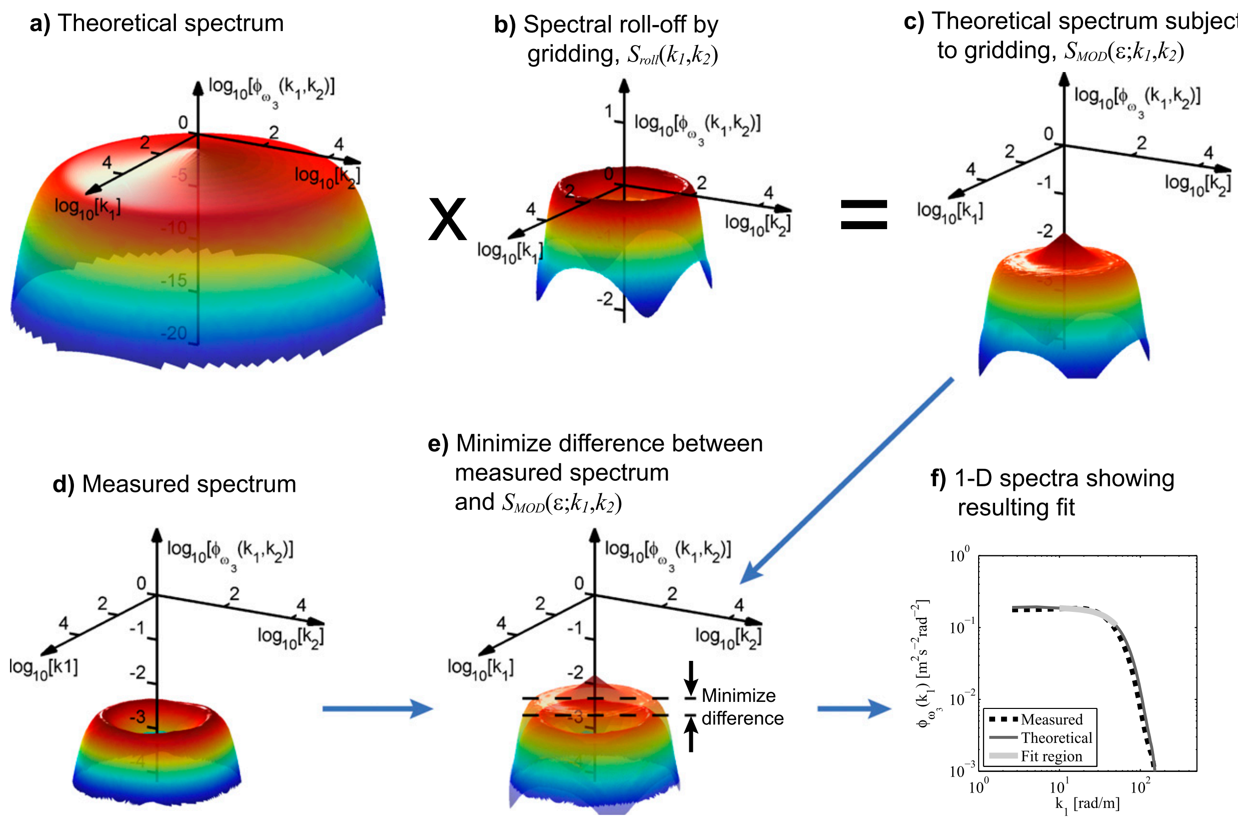

FIG. 6. Processing sequence for calculating dissipation from vorticity spectra. (a) 2D theoretical spectrum $\phi_{\omega_3}(\varepsilon; k_1, k_2)$ of vertical vorticity is calculated, using Eq. (7), based on an initial estimate of ε. (b) Spectral rolloff due to sampling $S_{\rm roll}(k_1, k_2)$ is calculated as in Eq. (11). (c) Theoretical spectrum is multiplied by $S_{\rm roll}(k_1, k_2)$ to calculate the theoretical spectrum subject to gridding $S_{\rm MOD}(\varepsilon; k_1, k_2)$, as in Eq. (12). (d) Directional wavenumber spectrum of vorticity is calculated as described in section 3c. (e) The squared difference between the measured spectrum and $S_{\rm MOD}(\varepsilon; k_1, k_2)$ is calculated over the wavenumber range $10 < k < 50$ rad m^{-1}. Steps (a),(c), and (e) are then repeated iteratively, with different initial values of ε, in order to minimize the difference between the measured and theoretical spectra. The value of ε corresponding to the minimum difference is then taken to be the surface dissipation. (f) Example 1D theoretical and measured spectra after spectral fitting is complete. Color scales are for visualization purposes only and are not consistent between subplots.

suppression of vertical velocities is two-dimensionality. It can be shown (Sutherland 2013, appendix B) that an equation analogous to Eq. (8) can be written for the case of 2D turbulence,

$$\phi_{\omega_3}(k_1) = \frac{2}{\pi}\int_0^\infty kE(k)\,dk_2 = \frac{2}{\pi}\int_{k_1}^\infty \frac{k^2E(k)}{(k^2-k_1^2)^{1/2}}\,dk. \quad (14)$$

Figure 5 also includes solutions of Eq. (14), showing considerable similarity between the theoretical vorticity spectra for 2D and 3D turbulence. Assuming 3D isotropic turbulence and using the vorticity spectrum technique for estimating dissipation will overestimate, by approximately a factor of 2, the TKE dissipation rate if the turbulence is actually 2D. Thus, the measurements as presented here could be considered to be an upper limit on the TKE dissipation at the sea surface.

Another concern is the observation that 2D wavenumber spectra of vorticity show a lobed structure, indicating a departure from the isotropy that was assumed in the derivations of Eqs. (7), (8), (9), and (14). This departure from isotropy in the spectra typically gave $\gamma_D < 0.25$ [see Eq. (6)] and has been neglected. For comparison, ε computed using azimuthally averaged isotropic versions of the measured spectra resulted in an average change of $-0.2\% \pm 3.0\%$ from ε computed using the full measured spectra.

5. Discussion

a. Comparison with the literature

To the best of our knowledge, the literature contains no other direct measurements of TKE dissipation at the wavy ocean surface on the scales resolved here. Nonetheless, some comparisons can still be made.

Measurements by Gemmrich (2010) used an upward-looking pulse-coherent acoustic Doppler profiler to study near-surface dissipation in the fetch-limited

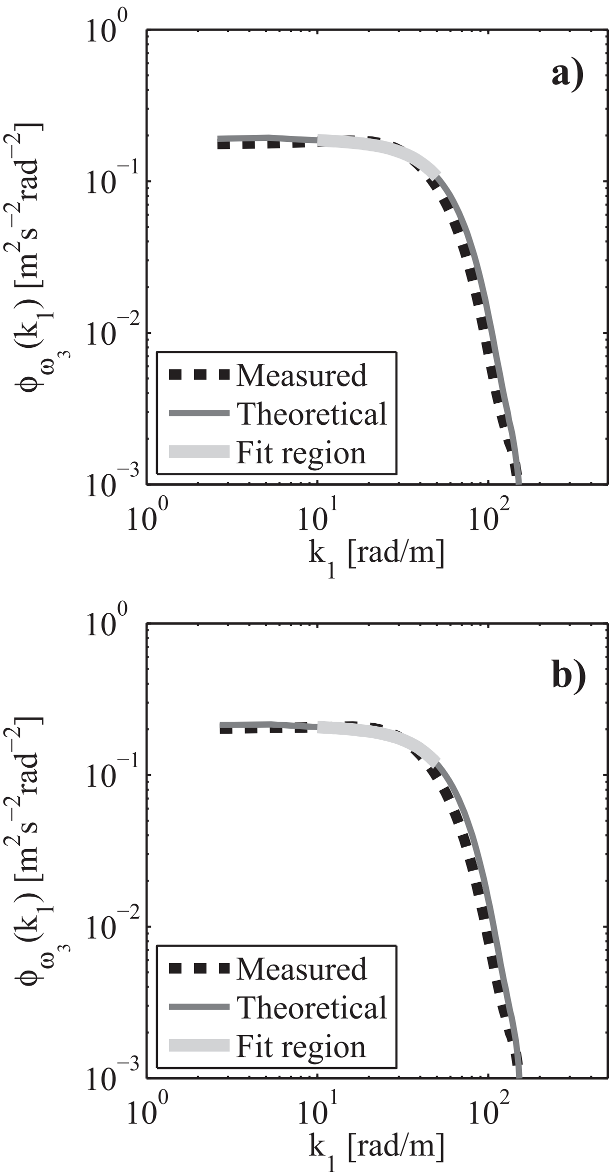

FIG. 7. The 20-min average 1D spectra corresponding to the 2D directional spectra shown in Fig. 3: (a) taken starting 0400 UTC 8 Sep 2009 and (b) taken starting 0500 UTC 8 Sep 2009. Dashed black lines are measured spectra and thin gray lines are theoretical spectra, including resolution rolloff $S_{\rm MOD}(\varepsilon; k_1)$. Thick light gray lines are $S_{\rm MOD}(\varepsilon; k_1)$ in the range of wavenumbers used for spectral fitting for calculation of surface TKE dissipation, described in section 4 (the same range of wavenumbers is indicated in Fig. 3a by a thick gray line).

($<$7 km), low wave ($H_s < 0.5$ m), low wave-age conditions of Lake Washington. Figure 8 shows his dissipation from the top 10 cm of the water column, plotted as a function of band-averaged wave saturation. The black and gray shapes are from Gemmrich (2010), and the colored shapes are from this work. The band-averaged saturation was defined as

$$B_b = \int_{\sigma_p}^{\sigma_u} \sigma^{-1} B(\sigma)\, d\sigma, \tag{15}$$

where σ is the radian frequency, σ_p is the spectral peak, σ_u is the upper limit of integration, and the saturation spectrum $B(\sigma) = \sigma^5 S_{\eta\eta}(\sigma)/2g^2$ is defined in terms of the frequency spectrum $S_{\eta\eta}(\sigma)$ (Phillips 1977, section 4.5). Gemmrich (2010) chose $\sigma_u = 4\sigma_p$, which he suggested would include all scales of breaking. For this work, in open-ocean conditions, the range of breaking was much larger. The upper integration limit was chosen based on the peak of the nondimensionalized $\Lambda(c)$ given in Fig. 4 of Sutherland and Melville (2013)—that peak is located at approximately $\hat{c} = 0.1$, where

$$\hat{c} = (c/\sqrt{gH_s})(gH_s/c_m^2)^{0.1}. \tag{16}$$

Solving for c and then mapping to radian frequency using the deep-water dispersion relation gives

$$\sigma_u = \frac{g}{0.1\sqrt{gH_s}}\left(\frac{gH_s}{c_m^2}\right)^{0.1}. \tag{17}$$

Note that there are significant contributions by breakers at $\hat{c} < 0.1$ that are not included in this definition. The stereo IR PIV data have not been separated into crest and trough components, but their mean values do fall between the crest and trough values of Gemmrich (2010). Also encouraging is that both sets of measurements appear to have a similar threshold value of $B_b \approx 0.01$, above which dissipation increases, presumably due to the onset of breaking.

b. *Dissipation by breaking*

A major goal of this work was to be able to measure surface dissipation in the presence of breaking waves. Figure 9 illustrates the effect of an example breaking wave on surface TKE dissipation. The top images in that figure show the breaking wave propagating through the field of view of one of the stereo IR cameras, and Fig. 9e shows the time series of surface dissipation corresponding to that same event. As the breaker passes, dissipation rapidly increases and then decays to the background level within approximately 5 s. The measured decay was fit with an exponential decay with a time constant of $0.6T_m$ (red curve) and a $(t/T_m)^{-1}$ fit (blue curve). Here, T_m is the mean wave period. The $(t/T_m)^{-1}$ temporal dependence of dissipation has been observed in laboratory experiments (Melville et al. 2002) for individual breaking events.

It is relatively easy to isolate the effect of a single large breaker on surface TKE dissipation, but the effects of

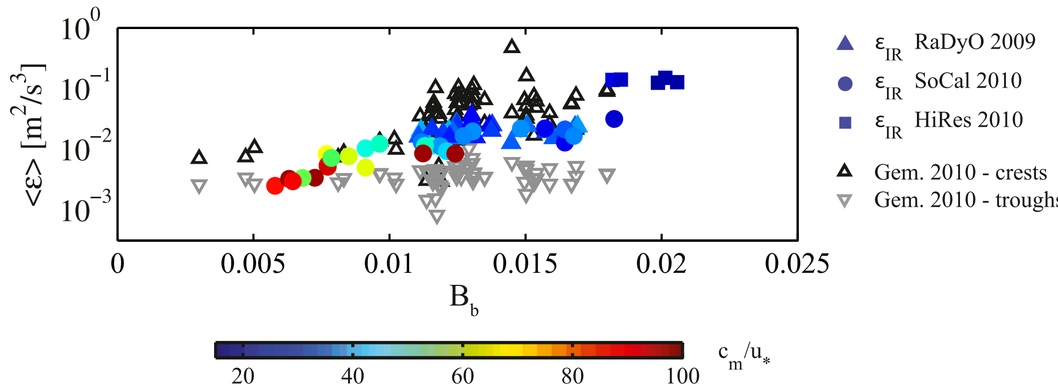

FIG. 8. Dependence of surface dissipation on band-averaged saturation B_b [see Eq. (15)]. Data from Gemmrich (2010) are 40-min averages of dissipation within 10 cm of the free surface. They are separated into measurements taken beneath wave crests (black up triangles) and wave troughs (gray down triangles). Stereo IR PIV measurements are 20-min averages, colored by wave age. Triangles are from RaDyO 2009 and circles are from SoCal 2010.

individual smaller breakers—of which many may populate the imagery at any given time—is more challenging. It is instead useful to examine breaking statistics. Sutherland and Melville (2013) used the stereo IR imagery described in this work to detect and track breaking waves at the sea surface. Sutherland and Melville (2015) were then able to combine the surface dissipation measurements taken here with subsurface turbulence measurements to estimate total near-surface dissipation. They found good agreement between total near-surface dissipation and dissipation by breaking in conditions where breaking was expected to be the dominant source of dissipation; that is, wave ages below $c_m/u_* = 40$ and winds above $U_{10} = 5\,\mathrm{m\,s^{-1}}$.

c. Alternate TKE estimates

In addition to comparing our dissipation estimates with values from the literature, it is also useful to attempt to derive dissipation using our same measurements but with a different set of assumptions. Here, we separate the surface velocity field into rotational and irrotational components using the Helmholtz decomposition. It is then possible to use the rotational velocity field directly to compute dissipation, rather than using the vorticity field as in section 4. The results are shown to be consistent.

1) HELMHOLTZ DECOMPOSITION

Separation of the horizontal component of the surface velocity field into its irrotational and rotational components, as in the 2D case of Eq. (2), is dependent on boundary conditions. For the following discussion, it is assumed that both vorticity and divergence vanish at infinity in the horizontal directions. It is then possible, following Corpetti et al. (2003), to compute irrotational and rotational components of the velocity as

$$\mathbf{u}_I = \mathscr{F}^{-1}\left[\mathbf{k}\cdot\hat{\mathbf{u}}(\mathbf{k})\frac{\mathbf{k}}{\|\mathbf{k}\|^2}\right] \tag{18}$$

and

$$\mathbf{u}_R = \mathscr{F}^{-1}\left[\mathbf{k}^{\perp}\cdot\hat{\mathbf{u}}(\mathbf{k})\frac{\mathbf{k}^{\perp}}{\|\mathbf{k}^{\perp}\|^2}\right], \tag{19}$$

respectively. Here, $\hat{\mathbf{u}}(\mathbf{k}) = \mathscr{F}[\mathbf{u}(\mathbf{x})]$ is the Fourier transform of $\mathbf{u}(\mathbf{x})$, $\mathscr{F}^{-1}$ indicates the inverse Fourier transform, $\mathbf{k} = (k_1, k_2)$ is the horizontal wavenumber, and $\mathbf{k}^{\perp} \equiv (-k_2, k_1)$. An alternative, mathematically equivalent, formulation is given in Smith (2008).

This decomposition was applied to the regridded surface horizontal velocity fields measured using the stereo IR PIV system. It was found that rotational velocity fields $\mathbf{u}_R$ separated in this manner captured an average of 97% of the vorticity variance of the original velocity field; that is,

$$\langle(\nabla\times\mathbf{u}_R)^2\rangle/\langle(\nabla\times\mathbf{u})^2\rangle \simeq 0.97, \tag{20}$$

suggesting that the underlying assumptions were valid. The separated rotational velocity field $\mathbf{u}_R$ was then assumed to be representative of turbulence for further analysis.

2) INERTIAL SUBRANGE FIT

The classical technique for calculating dissipation when the smallest scales are not fully resolved is to fit data to a Kolmogorov inertial subrange (ISR). Assuming homogeneous, isotropic turbulence, and that the scales observed are larger than the scale of dissipation (Kolmogorov scale) but smaller than the scale of energy input (outer scale), one-dimensional energy spectra have the form

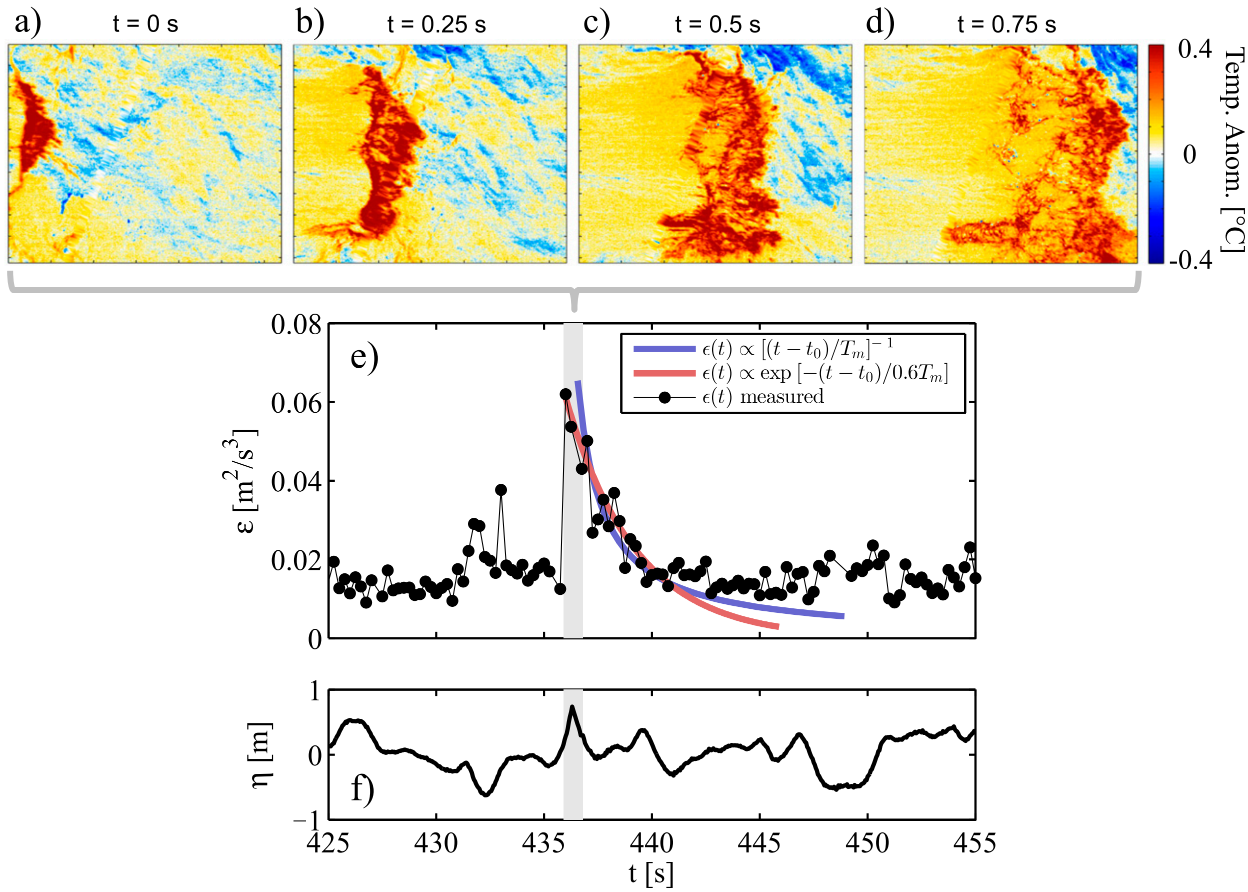

FIG. 9. Increased surface TKE dissipation due to a large breaking wave: (a)–(d) IR images of the sea surface separated by 0.25 s. Temperature anomaly scale is from $-0.4°$ (blue) to 0.4°C (red). Time series of (e) dissipation and (f) surface elevation as the breaker passes through the IR camera field of view. Blue line in (e) is the t^{-1} decay of dissipation found by Melville et al. (2002), and the red line is an exponential fit to the data having a decay time scale of $0.6T_m$. The shaded area is the duration during which the breaking front was in the field of view, and t_0 is taken to be the center of that period. The surface elevation is that of a 10 cm × 10 cm patch in the center of the image. The time axis is seconds since 2200 UTC 6 Dec 2010, during the SoCal 2010 experiment.

$$E_{11}(k_1) = \frac{18}{55} C\varepsilon^{2/3} k_1^{-5/3}, \tag{21}$$

and similarly

$$E_{22}(k_1) = \frac{24}{55} C\varepsilon^{2/3} k_1^{-5/3}. \tag{22}$$

In this notation, $E_{ii}(k_j)$ is the energy spectrum of velocity in the ith direction, taken over the jth spatial direction. The level of these spectra only depends on the TKE dissipation rate ε and a universal constant C, which has been experimentally determined to be $C = 1.5$ (Grant et al. 1962; Pope 2000, section 6.5).

Here, in order to exclude irrotational surface wave energy, only the rotational components $\mathbf{u}_R$ of gridded surface velocity were used. Surface velocity was separated into east (x) and north (y) components u and v, respectively. For each frozen image of surface velocity, along- and cross-velocity spectra were taken for both east and north components of velocity. These spectra were then substituted into Eqs. (21) and (22), and the equations were solved for the dissipation. This spectral fitting occurred over a wavenumber range $10 \le k \le 60\,\mathrm{rad\,m^{-1}}$. In isotropic turbulence, the direction chosen for k_1 is unimportant. Indeed, 20-min average dissipation values calculated using either Eq. (21) or (22) and with k_1 oriented either in the east or north direction were all typically within 10%—consistent with the departure from isotropy found in the vorticity spectra, section 3c.

3) INERTIAL SCALING BASED ON OUTER SCALES

Given the uncertainty of the existence of isotropic fields at the surface, it is useful to have an independent check on the use of such methods for calculating ε. The inertial, or large eddy, technique does not require an assumption of isotropy. Taylor (1935) noted that, at sufficiently high Reynolds numbers, ε is independent of viscosity and can be written as

$$\varepsilon = C_\varepsilon \frac{U'^3}{L}, \tag{23}$$

where L is the characteristic length scale, U' is the characteristic velocity scale, and C_ϵ is Taylor's dissipation constant (see also Tennekes and Lumley 1972, section 1.5). For high Reynolds numbers, C_ϵ asymptotes to a constant of order unity. Considerable effort in the literature has been applied to attempt to determine this constant precisely (e.g., Sreenivasan 1984, 1998), but the actual asymptotic value of the constant appears to not be a universal value, instead depending on the particular flow (Mazellier and Vassilicos 2008; Goto and Vassilicos 2009). Oceanographic measurements from Gargett (1999) found the constant of proportionality to be approximately equal to unity, within a factor of 2, when comparing large eddy estimates with direct measurements of dissipation. This inertial scaling has also been used with some success to scale surface wave energy dissipation by breaking (Drazen et al. 2008; Romero et al. 2012; Pizzo and Melville 2013; Grare et al. 2013; Deike et al. 2015; Melville and Fedorov 2015). In this work, the root-mean-square (RMS) rotational velocity $\langle u_R'^2 \rangle^{1/2}$ was used to define U', and the integral length scale of autocorrelation function of rotational velocity was used to define L—both being measured at the surface.

4) Comparison of methods

Measurements of surface dissipation from the vorticity spectral technique and from the two techniques based on the Helmholtz decomposition were found to be consistent. Figure 10 shows a comparison of the 20-min average dissipation calculated using the three methods.

Dissipation calculated using the inertial subrange fit is an average of 12% lower than that calculated using the vorticity spectrum technique. Close agreement is expected, as the vorticity spectrum technique is directly analogous to fitting the inertial subrange.

The large eddy technique produces dissipation values an average of 6% lower than the vorticity spectrum technique, but with considerable scatter. However, it should be noted that the large eddy technique is biased high, relative to the vorticity spectrum fit technique, for data taken during the SoCal 2010 experiment, and biased low for the RaDyO 2009 experiment. One potential explanation for this bias is that the field of view was larger for the RaDyO experiment than it was during the SoCal 2010 experiment, allowing the RaDyO experiment to find larger L values.

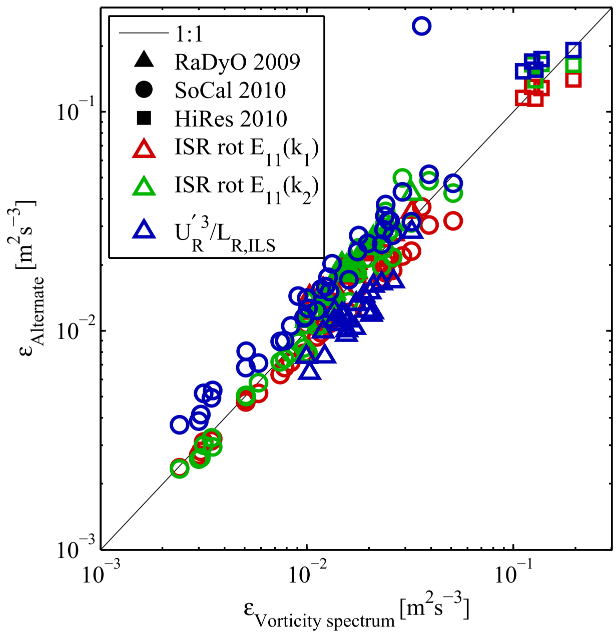

FIG. 10. Comparison of techniques for calculating ε at the surface. Each symbol corresponds to a 20-min average. The abscissa is dissipation calculated using the vorticity spectral fit method. Red and green symbols are for the values on the ordinate calculated using Eqs. (21) and (22), respectively (using the rotational velocity component). Blue symbols are for the values calculated using the inertial (large eddy) method. Triangles are data collected during RaDyO 2009, circles are data from SoCal 2010, and squares are data from HiRes 2010.

Each of the three methods uses a different set of assumptions. Both the inertial subrange fit technique and the vorticity spectral fit technique assume the presence of homogeneous isotropic turbulence. However, application of the inertial subrange fit method also relies on the Helmholtz decomposition, which assumes that vorticity and divergence of the velocity field vanish at infinity. The inertial scaling technique does not require isotropy, but it does make use of the Helmholtz decomposition and assumes that the length scale L is far larger than the dissipative scales. The relative agreement between the three methods, over almost two orders of magnitude of dissipation range, lends credibility to the calculations.

6. Conclusions

This work has introduced a new technique for measuring turbulence at the sea surface. Surface morphology and velocity were measured using a stereo pair of infrared cameras. Using the vorticity of the surface velocity field, it was possible to measure TKE dissipation using rotational turbulent fluctuations, without contamination by irrotational wave velocities. This technique removed the principle difficulties of sampling turbulence near the air–sea boundary, namely, the separation of waves and turbulence, and instrument wake contamination.

Calculated surface dissipation values were found to be consistent with the small amount of reasonably comparable literature (Fig. 8). Surface dissipation was found to strongly depend on wave spectral saturation B_b. Surface dissipation was also found to be strongly modulated by wave breaking (Fig. 9). Testing the method over a broad range of environmental conditions showed good self-consistency (see Fig. 10).

Moving forward, it is important to connect these new measurements of TKE dissipation at the sea surface with subsurface measurements. This permits improved estimates of total TKE dissipation in the upper ocean (Sutherland and Melville 2015).

Acknowledgments. We are grateful for the engineering and field support of Nick Statom and Luc Lenain, without whose hard work and expertise these measurements would not have been possible. We also thank Tom Golfinos, Bill Gaines, and the crew of R/P *FLIP*, who were always willing to do whatever it took, in often challenging conditions, to help us take these measurements. We thank Fabrice Veron and Zachary VanKirk for providing the stereo matching routine and for assisting with data collection during the HiRes 2010 experiment; and Luc Lenain for the many useful discussions regarding video analysis. Two anonymous reviewers contributed significantly to the clarity of this work, and we are grateful for their efforts. This research was conducted under grants to WKM from the Office of Naval Research (Physical Oceanography, HiRes and RaDyO DRIs) and the National Science Foundation (Ocean Sciences). During the revision and final preparation of this paper, PS was supported at Laboratoire d'Océanographie et du Climat by grants from the European Commission (PI: Jean-Claude Gascard).

APPENDIX

Stereo PIV Processing Sequence

Image analysis in this work made use of the following processing sequence.

1) *Initial preparation.* Most images contained a data and support cable for subsurface instrumentation. Potential image pixels on this line were found using a Roberts edge detection algorithm (Gonzalez et al. 2009, 543–545). Because of the large number of nonline pixels detected, a random sample consensus (RANSAC) technique was used to fit a line to these points (see, e.g., Hartley and Zisserman 2003, 117–121). A line through this fit (10 pixels wide for RaDyO 2009 data, 20 pixels wide for SoCal 2010 and HiRes 2010 data) was removed from the image and filled in using a linear interpolation from the surrounding pixels.
2) *Mean removal.* For each 20-min IR video record, a mean image was calculated by averaging 500 images equally spaced in time, and this mean image was subtracted from each individual image to retrieve the temperature anomaly, which was used for all subsequent analysis.
3) *Calibration and image rectification.* During the RaDyO 2009 experiment, the camera setup was calibrated using a checkerboard-patterned calibration card and applying the Bouguet (2010) Camera Calibration Toolbox for MATLAB. Because of an inability to use the checkerboard during the SoCal 2010 and HiRes 2010 experiments, those images were calibrated using the Fusiello and Irsara (2008) uncalibrated rectification MATLAB toolbox with manually selected point matches. Epipolar rectification (Ma et al. 2004) was then performed on all images. This consists of a set of projective transformations that result in image pairs where epipolar lines follow horizontal scan lines; that is, any image feature will be at the same vertical pixel in the left and right images, allowing the search for stereo correspondences to be carried out in one dimension.
4) *Disparity calculation.* Stereo feature matching was applied to epipolar-rectified image pairs. Disparity maps were created using a multilevel normalized cross-correlation matching routine developed specifically for surface wave field reconstruction by Fabrice Veron and Zachary VanKirk at the University of Delaware. Cascading windows were square with 256-, 128-, 64-, 32-, 16-, and 8-pixel edges with 50% overlap. This resulted in a final resolution of eight pixels or approximately 5 cm. Image disparity was calculated for every second image, resulting in a frame rate of 20 Hz.
5) *3D triangulation.* Stereo reconstruction of the sea surface from disparity maps followed standard techniques developed for visible imagery (Hartley and Zisserman 2003). 3D points were triangulated using the Bouguet (2010) toolbox. A curvature resulting in approximately 10-cm displacement over 2 m remained in the mean reconstructed surface in the SoCal 2010 and HiRes 2010 experiments due to uncorrected lens distortion. To remove that curvature, a 2D parabola was fitted to each image, and those parabolas were averaged over 20 min of images. The 20-min mean curvature was then removed from each image. The

validity of this correction was checked by ensuring that the mean reconstructed surface was flat and that different locations on the final reconstructed water surface showed a constant variance in vertical displacement.

6) *Thermal structure PIV*. Independent of the stereo processing, PIV was applied to the unrectified images. Feature tracking was performed on images separated by 0.05 s, using a normalized cross-correlation technique with cascading window sizes of 64, 32, 16, and 8 pixels. The algorithm used is a modified version of the publicly available PIV Laboratory software (Thielicke and Stamhuis 2010) and is capable of detecting subpixel displacements, allowing displacements for each window to be calculated theoretically to within less than 0.1 pixel (approximately 0.6 mm). The algorithm was tested on synthetic data to ensure that it could convincingly track features in the IR video data used here over a range of scales and was found to have a mean square error of approximately 1.7 pixels. This PIV processing was only applied to the camera with a higher signal-to-noise ratio in each experiment—that was the left camera during RaDyO 2009 and SoCal 2010, and the right camera during Hires 2010.
7) *3D velocity calculation.* Each 3D point computed in the stereo processing corresponds to a specific pixel location in the original image. Using the separation between points in both pixel and real coordinates, it is possible to derive a relation between pixels and meters for every pixel location in the image—that relation is then used to convert PIV measurements of pixels per second to meters per second.
8) *Gridding data.* Further processing required that velocity and vorticity measurements be interpolated to a uniform grid. Linear interpolation was performed using a regridding resolution of 2 cm, approximately twice the 95th percentile PIV sampling resolution of an image sequence. Since the edges of the stereo reconstructions were not uniform, a smaller subwindow of the gridded data was used for calculation of spectra and other statistics. This window was typically 2 m × 2 m, and it removed the problem of having missing data at the edges of the data fields.

REFERENCES

Agrawal, Y. C., E. A. Terray, M. A. Donelan, P. A. Hwang, A. J. Williams III, W. M. Drennan, K. K. Kahma, and S. A. Kitaigorodskii, 1992: Enhanced dissipation of kinetic energy beneath surface waves. *Nature,* **359,** 219–220, doi:10.1038/359219a0.

Anis, A., and J. Moum, 1992: The superadiabatic surface layer of the ocean during convection. *J. Phys. Oceanogr.,* **22,** 1221–1227, doi:10.1175/1520-0485(1992)022<1221:TSSLOT>2.0.CO;2.

Antonia, R. A., L. W. B. Browne, and D. A. Shah, 1988: Characteristics of vorticity fluctuations in a turbulent wake. *J. Fluid Mech.,* **189,** 349–365, doi:10.1017/S0022112088001053.

Banner, M. L., I. S. F. Jones, and J. C. Trinder, 1989: Wavenumber spectra of short gravity waves. *J. Fluid Mech.,* **198,** 321–344, doi:10.1017/S0022112089000157.

Benetazzo, A., 2006: Measurements of short water waves using stereo matched image sequences. *Coastal Eng.,* **53,** 1013–1032, doi:10.1016/j.coastaleng.2006.06.012.

Bouguet, J.-Y., 2010: Camera calibration toolbox for MATLAB. Access 6 January 2009. [Available online at www.vision.caltech.edu/bouguetj/calib_doc/.]

Chickadel, C., S. Talke, A. Horner-Devine, and A. Jessup, 2011: Infrared-based measurements of velocity, turbulent kinetic energy, and dissipation at the water surface in a tidal river. *IEEE Geosci. Remote Sens. Lett.,* **8,** 849–853, doi:10.1109/LGRS.2011.2125942.

Corpetti, T., E. Mémin, and P. Pérez, 2003: Extraction of singular points from dense motion fields: An analytic approach. *J. Math. Imaging Vision,* **19,** 175–198, doi:10.1023/A:1026352203836.

Deike, L., S. Popinet, and W. K. Melville, 2015: Capillary effects on wave breaking. *J. Fluid Mech.,* **769,** 541–569, doi:10.1017/jfm.2015.103.

Dickey, T., and Coauthors, 2012: Introduction to special section on recent advances in the study of optical variability in the near-surface and upper ocean. *J. Geophys. Res.,* **117,** C00H20, doi:10.1029/2012JC007964.

Drazen, D. A., W. K. Melville, and L. Lenain, 2008: Inertial scaling of dissipation in unsteady breaking waves. *J. Fluid Mech.,* **611,** 307–332, doi:10.1017/S0022112008002826.

Drennan, W., M. Donelan, E. Terray, and K. Katsaros, 1996: Oceanic turbulence dissipation measurements in SWADE. *J. Phys. Oceanogr.,* **26,** 808–815, doi:10.1175/1520-0485(1996)026<0808:OTDMIS>2.0.CO;2.

Fusiello, A., and L. Irsara, 2008: Quasi-Euclidean uncalibrated epipolar rectification. *19th International Conference on Pattern Recognition, 2008,* IEEE, 4 pp., doi:10.1109/ICPR.2008.4761561.

Garbe, C. S., H. Spies, and B. Jähne, 2003: Estimation of complex motion from thermographic image sequences. *Thermosense XXV,* K. E. Cramer, and X. P. Maldague, Eds., International Society for Optical Engineering (SPIE Proceedings, Vol. 5073), 303–317.

Gargett, A. E., 1989: Ocean turbulence. *Annu. Rev. Fluid Mech.,* **21,** 419–451, doi:10.1146/annurev.fl.21.010189.002223.

——, 1999: Velcro measurement of turbulence kinetic energy dissipation rate ε. *J. Atmos. Oceanic Technol.,* **16,** 1973–1993, doi:10.1175/1520-0426(1999)016<1973:VMOTKE>2.0.CO;2.

Gemmrich, J., 2010: Strong turbulence in the wave crest region. *J. Phys. Oceanogr.,* **40,** 583–595, doi:10.1175/2009JPO4179.1.

Gerbi, G. P., J. H. Trowbridge, E. A. Terray, A. J. Plueddemann, and T. Kukulka, 2009: Observations of turbulence in the ocean surface boundary layer: Energetics and transport. *J. Phys. Oceanogr.,* **39,** 1077–1096, doi:10.1175/2008JPO4044.1.

Gonzalez, R. C., R. E. Woods, and S. L. Eddins, 2009: *Digital Image Processing Using MATLAB.* 2nd ed. Gatesmark Publishing, 827 pp.

Goto, S., and J. C. Vassilicos, 2009: The dissipation rate coefficient of turbulence is not universal and depends on the internal stagnation point structure. *Phys. Fluids,* **21,** 035104, doi:10.1063/1.3085721.

Grant, H. L., R. W. Stewart, and A. A. Moilliet, 1962: Turbulence spectra from a tidal channel. *J. Fluid Mech.,* **12,** 241–268, doi:10.1017/S002211206200018X.

Grare, L., W. L. Peirson, H. Branger, J. W. Walker, J.-P. Giovanangeli, and V. Makin, 2013: Growth and dissipation of wind-forced, deep-water waves. *J. Fluid Mech.,* **722,** 5–50, doi:10.1017/jfm.2013.88.

Hartley, R., and A. Zisserman, 2003: *Multiple View Geometry in Computer Vision.* 2nd ed. Cambridge University Press, 655 pp.

Hilsenstein, V., 2005: Surface reconstruction of water waves using thermographic stereo imaging. *Proceedings of Image and Vision Computing New Zealand (IVCNZ 2005),* B. McCane, Ed., University of Otago, 102–107.

Jähne, B., J. Klinke, and S. Waas, 1994: Imaging of short ocean wind waves: A critical theoretical review. *J. Opt. Soc. Amer.,* **11A,** 2197–2209, doi:10.1364/JOSAA.11.002197.

Kitaigorodskii, S. A., and J. L. Lumley, 1983: Wave–turbulence interactions in the upper ocean. Part I: The energy balance of the interacting fields of surface wind waves and wind-induced three-dimensional turbulence. *J. Phys. Oceanogr.,* **13,** 1977–1987, doi:10.1175/1520-0485(1983)013<1977:WTIITU>2.0.CO;2.

——, M. Donelan, J. L. Lumley, and E. Terray, 1983: Wave–turbulence interactions in the upper ocean. Part II: Statistical characteristics of wave and turbulent components of the random velocity field in the marine surface layer. *J. Phys. Oceanogr.,* **13,** 1988–1999, doi:10.1175/1520-0485(1983)013<1988:WTIITU>2.0.CO;2.

Lindborg, E., 2007: Horizontal wavenumber spectra of vertical vorticity and horizontal divergence in the upper troposphere and lower stratosphere. *J. Atmos. Sci.,* **64,** 1017–1025, doi:10.1175/JAS3864.1.

Lumley, J. L., and E. A. Terray, 1983: Kinematics of turbulence convected by a random wave field. *J. Phys. Oceanogr.,* **13,** 2000–2007, doi:10.1175/1520-0485(1983)013<2000:KOTCBA>2.0.CO;2.

Ma, Y., S. Soatto, J. Koseckà, and S. S. Sastry, 2004: *An Invitation to 3-D Vision: From Images to Geometric Models*. Interdisciplinary Applied Mathematics, Vol. 26, Springer, 528 pp., doi:10.1007/978-0-387-21779-6.

Mazellier, N., and J. C. Vassilicos, 2008: The turbulence dissipation constant is not universal because of its universal dependence on large-scale flow topology. *Phys. Fluids,* **20,** 015101, doi:10.1063/1.2832778.

Melville, W. K., 1994: Energy dissipation in breaking waves. *J. Phys. Oceanogr.,* **24,** 2041–2049, doi:10.1175/1520-0485(1994)024<2041:EDBBW>2.0.CO;2.

——, 1996: The role of surface-wave breaking in air-sea interaction. *Annu. Rev. Fluid Mech.,* **28,** 279–321, doi:10.1146/annurev.fl.28.010196.001431.

——, and A. Fedorov, 2015: The equilibrium dynamics and statistics of gravity–capillary waves. *J. Fluid Mech.,* **767,** 449–466, doi:10.1017/jfm.2014.740.

——, F. Veron, and C. J. White, 2002: The velocity field under breaking waves: Coherent structures and turbulence. *J. Fluid Mech.,* **454,** 203–233, doi:10.1017/S0022112001007078.

Mollo-Christensen, E., 1968: Wind tunnel test of the superstructure of the R/V Flip for assessment of wind field distortion. MIT Fluid Dynamics Laboratory, 34 pp.

Osborn, T., D. M. Farmer, S. Vagle, S. A. Thorpe, and M. Cure, 1992: Measurements of bubble plumes and turbulence from a submarine. *Atmos.–Ocean,* **30,** 419–440, doi:10.1080/07055900.1992.9649447.

Phillips, O. M., 1977: *The Dynamics of the Upper Ocean.* 2nd ed. Cambridge University Press, 336 pp.

Pizzo, N. E., and W. K. Melville, 2013: Vortex generation by deep-water breaking waves. *J. Fluid Mech.,* **734,** 198–218, doi:10.1017/jfm.2013.453.

Pope, S. B., 2000: *Turbulent Flows.* Cambridge University Press, 802 pp.

Rocholz, R., S. Wanner, U. Schimpf, and B. Jähne, 2011: Combined visualization of wind waves and water surface temperature. *Contributions from the International Symposium on Gas Transfer at Water Surfaces,* S. Komori, W. McGillis, and R. Kurose, Eds., Kyoto University Press, 496–506.

Romero, L., W. K. Melville, and J. M. Kleiss, 2012: Spectral energy dissipation due to surface-wave breaking. *J. Phys. Oceanogr.,* **42,** 1421–1444, doi:10.1175/JPO-D-11-072.1.

Saddoughi, S. G., and S. V. Veeravalli, 1994: Local isotropy in turbulent boundary layers at high Reynolds number. *J. Fluid Mech.,* **268,** 333–372, doi:10.1017/S0022112094001370.

Shemdin, O. H., H. M. Tran, and S. C. Wu, 1988: Directional measurement of short ocean waves with stereophotography. *J. Geophys. Res.,* **93,** 13 891–13 901, doi:10.1029/JC093iC11p13891.

Shen, L., and D. K. P. Yue, 2001: Large-eddy simulation of free-surface turbulence. *J. Fluid Mech.,* **440,** 75–116, doi:10.1017/S0022112001004669.

Smith, J. A., 2008: Vorticity and divergence of surface velocities near shore. *J. Phys. Oceanogr.,* **38,** 1450–1468, doi:10.1175/2007JPO3865.1.

——, and K. F. Rieder, 1997: Wave induced motion of flip. *Ocean Eng.,* **24,** 95–110, doi:10.1016/0029-8018(96)00008-X.

Soloviev, A., N. Vershinsky, and V. Bezverchnii, 1988: Small-scale turbulence measurements in the thin surface layer of the ocean. *Deep-Sea Res.,* **35A,** 1859–1874, doi:10.1016/0198-0149(88)90113-6.

Sreenivasan, K. R., 1984: On the scaling of the turbulence energy dissipation rate. *Phys. Fluids,* **27,** 1048, doi:10.1063/1.864731.

——, 1998: An update on the energy dissipation rate in isotropic turbulence. *Phys. Fluids,* **10,** 528, doi:10.1063/1.869575.

Stewart, R. W., and H. L. Grant, 1962: Determination of the rate of dissipation of turbulent energy near the sea surface in the presence of waves. *J. Geophys. Res.,* **67,** 3177–3180, doi:10.1029/JZ067i008p03177.

Sutherland, P., 2013: On breaking waves and turbulence at the air-sea interface. Ph.D. dissertation, Scripps Institution of Oceanography, University of California, San Diego, 117 pp.

——, and W. K. Melville, 2013: Field measurements and scaling of ocean surface wave-breaking statistics. *Geophys. Res. Lett.,* **40,** 3074–3079, doi:10.1002/grl.50584.

——, and ——, 2015: Field measurements of surface and near-surface turbulence in the presence of breaking waves. *J. Phys. Oceanogr.,* **45,** 943–965, doi:10.1175/JPO-D-14-0133.1.

Taylor, G. I., 1935: Statistical theory of turbulence. *Proc. Roy. Soc. London,* **151A,** 421–444, doi:10.1098/rspa.1935.0158.

Tennekes, H., and J. L. Lumley, 1972: *A First Course in Turbulence.* MIT Press, 300 pp.

Terray, E. A., M. A. Donelan, Y. C. Agrawal, W. M. Drennan, K. K. Kahma, A. J. Williams III, P. A. Hwang, and S. A. Kitaigorodskii, 1996: Estimates of kinetic energy dissipation under breaking waves. *J. Phys. Oceanogr.,* **26,** 792–807, doi:10.1175/1520-0485(1996)026<0792:EOKEDU>2.0.CO;2.

Thielicke, W., and E. J. Stamhuis, 2010: PIVlab—Time-resolved digital particle image velocimetry tool for MATLAB. Accessed 17

August 2011. [Available online at http://pivlab.blogspot.com/.]

Trowbridge, J. H., 1998: On a technique for measurement of turbulent shear stress in the presence of surface waves. *J. Atmos. Oceanic Technol.,* **15,** 290–298, doi:10.1175/1520-0426(1998)015<0290:OATFMO>2.0.CO;2.

Turney, D. E., A. Andere, and S. Banerjee, 2009: A method for three-dimensional interfacial particle image velocimetry (3D-IPIV) of an air–water interface. *Meas. Sci. Technol.,* **20,** 045403, doi:10.1088/0957-0233/20/4/045403.

Veron, F., W. K. Melville, and L. Lenain, 2008: Infrared techniques for measuring ocean surface processes. *J. Atmos. Oceanic Technol.,* **25,** 307–326, doi:10.1175/2007JTECHO524.1.

——, ——, and ——, 2009: Measurements of ocean surface turbulence and wave–turbulence interactions. *J. Phys. Oceanogr.,* **39,** 2310–2323, doi:10.1175/2009JPO4019.1.